THE JOURNAL OF BIOLOGICAL CHEMISTRY VOL. 286, NO. 32, pp. 28265–28275, August 12, 2011
Printed in the U.S.A.

Structure and Mechanism of the Saposin-like Domain of a Plant Aspartic Protease*

Received for publication, April 25, 2011, and in revised form, May 27, 2011 Published, JBC Papers in Press, June 15, 2011, DOI 10.1074/jbc.M111.252619

Brian C. Bryksa[‡], Prasenjit Bhaumik[§], Eugenia Magracheva[¶], Dref C. De Moura[‡], Martin Kurylowicz[‖], Alexander Zdanov[§†], John R. Dutcher[‖], Alexander Wlodawer[§], and Rickey Y. Yada[‡1]

From the Departments of [‡]Food Science and [‖]Physics, University of Guelph, Guelph, Ontario N1G 2W1, Canada and the [§]Protein Structure Section, Macromolecular Crystallography Laboratory, and the [¶]Basic Research Program, SAIC-Frederick, NCI, National Institutes of Health, Frederick, Maryland 21702

Many plant aspartic proteases contain an additional sequence of ~100 amino acids termed the plant-specific insert, which is involved in host defense and vacuolar targeting. Similar to all saposin-like proteins, the plant-specific insert functions via protein-membrane interactions; however, the structural basis for such interactions has not been studied, and the nature of plant-specific insert-mediated membrane disruption has not been characterized. In the present study, the crystal structure of the saposin-like domain of potato aspartic protease was resolved at a resolution of 1.9 Å, revealing an open V-shaped configuration similar to the open structure of human saposin C. Notably, vesicle disruption activity followed Michaelis-Menten-like kinetics, a finding not previously reported for saposin-like proteins including plant-specific inserts. Circular dichroism data suggested that secondary structure was pH-dependent in a fashion similar to influenza A hemagglutinin fusion peptide. Membrane effects characterized by atomic force microscopy and light scattering indicated bilayer solubilization as well as fusogenic activity. Taken together, the present study is the first report to elucidate the membrane interaction mechanism of plant saposin-like domains whereby pH-dependent membrane interactions resulted in bilayer fusogenic activity that probably arose from a viral type pH-dependent helix-kink-helix motif at the plant-specific insert N terminus.

Aspartic proteases (APs)[2] are characterized by a common bilobal tertiary structure containing two catalytic aspartic acid residues (Asp^{32} and Asp^{215} in pepsin) within an active site cleft (1, 2). They are found in all higher organisms, and their respective roles are well established, although structural and functional characteristics of APs in plants are least understood. Of practical interest among plant APs are their roles in plant pathogen resistance (3) as well as in senescence and postharvest physiology (4, 5). Plant APs share the common AP bilobal structure; however, some contain an additional sequence of ~100 residues inserted within the C-terminal primary structure. These additional amino acids unique to plant APs (6–8) create an extra domain protruding from the canonical AP molecule (9–11). This structural oddity among APs is called the plant-specific insert (PSI), also known as the plant-specific sequence, which belongs to the saposin-like protein (SAPLIP) family (12, 13). Plant APs are found in either monomeric or heterodimeric forms (9, 14); the latter result from post-translational proteolysis, which includes the removal of part or all of the PSI, whereas the PSI is retained in monomeric plant APs (6, 8).

In general, members of the SAPLIP family have various physiological functions, all of which entail membrane interaction (14–16) manifested in three principal ways: membrane binding, membrane perturbation without permeabilization, and membrane permeabilization (15). Examples of SAPLIP functions include roles in exohydrolase degradation of sphingolipids in the lysosome (saposins) (17), antimicrobial activity (granulysin and NK-lysin) (18), tumor lysis (NK-lysin) (19), pulmonary surfactant surface tension regulation (surfactant protein B) (20), and bacterial/eukaryotic cell lysis (amoebapores) (21).

Fusion of cellular lipid membranes is an essential process in all forms of life (22), and the mechanism by which membrane fusion occurs, a process typically catalyzed by proteins, continues to be unraveled (23). Merely bringing membranes in proximity to one another is insufficient for fusion (23), and the nature of fusion peptide structures is critical to fusogenic function (24–26). Disordering of bilayers by fusion proteins, thought to be a critical first step in the catalysis of bilayer fusion (26), results in an increased rate of energetically unfavorable hydrophobic lipid tail protrusion (23). The fusion transition state involves contact formation between lipid tails of opposite bilayers within the intervening hydrophilic region (23), resulting in stalk formation(s) between the two disordered bilayer patches (23, 27). Dimerization of helical structures is part of the saposin-mediated bilayer fusion, transfer, and solubilizing mechanisms (28–30), and these structural rearrangements take place after release from the parent molecule (prosaposin) (16).

* This work was supported, in whole or in part, by the Intramural Research Program of the National Institutes of Health, NCI. This work was also supported by the Natural Sciences and Engineering Research Council of Canada, the Canada Research Chairs Program, and the Center for Cancer Research.

The atomic coordinates and structure factors (code 3RFI) have been deposited in the Protein Data Bank, Research Collaboratory for Structural Bioinformatics, Rutgers University, New Brunswick, NJ (http://www.rcsb.org/).

† Deceased May 19, 2010.

[1] To whom correspondence should be addressed: Dept. of Food Science, University of Guelph, Guelph, Ontario N1G 2W1, Canada. Fax: 519-824-6631; E-mail: ryada@uoguelph.ca.

[2] The abbreviations used are: AP, aspartic protease; Trx, recombinant *E. coli* thioredoxin; PSI, plant-specific insert; SAPLIP, saposin-like protein; StAP, *S. tuberosum* aspartic proteinase; LUV, large unilamellar vesicle; PC, phosphatidylcholine; PE, phosphatidylethanolamine; PS, phosphatidylserine; PL, phospholipid; AFM, atomic force microscopy; r.m.s., root mean square; SNARE, soluble *N*-ethylmaleimide-sensitive factor attachment protein receptor.

The SAPLIP domains of plant APs display membrane permeabilizing activity independent of its "parent" protein (14, 31), and they probably act independently (post-proteolytic processing) as a part of the plant defense mechanism against fungal pathogens (3, 32). Like PSIs of heterodimeric plant APs, saposins are also expressed as a proprotein and are subsequently processed via proteolytic cleavage (15), resulting in distinct, active tertiary structures consisting of stable helical and coil secondary structures (15, 28, 33–35).

Recently, recombinantly produced PSI of *Solanum tuberosum* aspartic proteinase (StAP) was shown to kill human pathogens as well as to inhibit fungal sporulation via interaction with and permeabilizaton of microbial plasma membranes (32). Understanding the structural basis for newly characterized antifungal activities is important in the development of novel therapeutic drugs for the treatment of fungal infections (36) in immunocompromised patients (37, 38). Furthermore, we propose that understanding structure-function relationships involving PSI-membrane interactions may have relevance to non-plant membrane-bound APs (*e.g.* memapsins 1 and 2) implicated in Alzheimer's disease beyond the direct elucidation of SAPLIP primary functions. Using StAP PSI as a model system, the present study characterizes the structure of a plant AP PSI as it relates to membrane interactions. The observed saposin C-like tertiary structure and saposin B-like fusogenic activity and the apparent catalysis of energetically unfavorable membrane bilayer disruption and fusion via a pH-dependent helix fusion peptide motif at the PSI N terminus are discussed.

EXPERIMENTAL PROCEDURES

Materials—A *PSI* synthetic gene optimized for expression in *Escherichia coli* was purchased from Mr. Gene GmbH (Regensburg, Germany). Plasmids pET19b(+) and pET32b(+), *E. coli* Rosetta-gami B (DE3)pLysS, and u-MAC™ columns were obtained from EMD Biosciences (San Diego, CA). *E. coli* TOP10F′ was from Invitrogen. The GenElute™ plasmid miniprep kit was obtained from Sigma-Aldrich. The QIAquick® PCR purification kit and QIAquick® gel extraction kit were from Qiagen (Germantown, MD). Restriction enzymes, T4 DNA ligase, and *Pfu* DNA polymerase were obtained from Fermentas Life Sciences (Burlington, Canada). Primers were synthesized by Sigma Genosys (Oakville, Canada), and thrombin was purchased from Fisher. The RPC column was from GE Healthcare. Phospholipids were from Avanti Polar Lipids (Alabaster, AL).

Construction of Expression Vector pET32z-PSI—Two constructs, a 6.0-kb construct named *pET19b-PSI* and a 6.2-kb construct named *pET32z-PSI*, were made for the expression of PSI and thioredoxin-PSI fusion protein (Trx-PSI), respectively, in *E. coli*. For *pET19b-PSI*, the *PSI* insert was amplified using primers FwdPSINdeI (5′-CATATGATTGTAAGCATGGAGTGTAAAACC) and RevPSIXhoI (5′-ATCTCGAGTTACGGGATTTTTTCACACAGTTG), followed by ligation between the NdeI and XhoI restriction sites. The *pET32z-PSI* construct was made using the *PSI* insert amplified using primers FwdPSINcoI (5′-ATCCATGGCGATTGTAAGCATGGAGTGTAAAACC) and RevPSIXhoI, followed by ligation between the NcoI and XhoI restriction sites of pET32z, a modified version of pET32b that contains a deletion between the thrombin cut site and the end of the enterokinase cut site. Each construct was transformed into *E. coli* TOP10F′ using the method of Hanahan (39).

Protein Expression—Overnight cultures of *E. coli* BL21 (DE3)pLysS or Rosetta-gami B (DE3)pLysS transformed with either *pET19b-PSI* or *pET32z-PSI* were used to express PSI as per the manufacturer's instructions. Cells were harvested by centrifugation at 4,500 × *g* for 10 min at 4 °C and stored at −20 °C until further use. Frozen cells were thawed at room temperature and resuspended in 20 ml of 20 mM Tris-Cl, pH 7.5. Suspensions were incubated at room temperature for 1 h with gentle shaking, and the resulting cell lysates were centrifuged at 21,000 × *g* for 30 min at 4 °C to remove insoluble matter.

Protein Purification—The following applies only to Trx-PSI fusion protein purification because pET19b-derived PSI was expressed at far lower concentrations and thus was not pursued to purity. Protein purification was performed using an AKTA™ FPLC system (GE Healthcare). Cell lysate soluble fractions were applied to five 1-ml u-MAC columns in series (EMD Biosciences, San Diego, CA) equilibrated with 300 mM NaCl, 20 mM imidazole in 50 mM sodium phosphate, pH 7.4 (binding buffer), followed by washing with the same buffer until a steady base line was obtained. Samples were eluted with 300 mM NaCl, 250 mM imidazole in 50 mM sodium phosphate, pH 7.4, and then dialyzed in 20 mM Tris-Cl, pH 7.4. Thrombin was added to the dialysates at a 1:2000 mass ratio for incubation at room temperature for at least 12 h followed by reapplication of samples to u-MAC in binding buffer three times consecutively at 2 ml/min to remove the Trx fusion tag. Flow-through was collected, dialyzed as above, and then applied to a 1-ml MonoQ column (GE Healthcare) and separated using a 0–500 mM NaCl gradient in 10 mM Tris-Cl, pH 7.4. Eluent sample was further purified and desalted on a 3-ml RPC column (GE Healthcare); washed with 2% acetonitrile, 0.065% TFA; and eluted with a 90-ml gradient (80% acetonitrile, 0.05% TFA elution buffer). The PSI peak, verified by SDS-PAGE and amino acid analysis (Advanced Protein Analysis Center, Hospital for Sick Children, Toronto, Canada), was collected and placed under vacuum in a Centrivap (Labconco Corp., Kansas City, MO) for 1 h at room temperature to remove the majority of the acetonitrile followed by dialysis against 4 × 1 liter of 5 mM Tris-Cl, pH 7.4, using 1000 Dalton molecular mass cut-off dialysis tubing.

SDS-PAGE—Tris/glycine-buffered SDS-PAGE was conducted according to the method of Laemmli (40) in a Mini-Protean III electrophoresis cell (Bio-Rad). Gels were stained with GelCode Blue® (Pierce) and were analyzed for band size and relative intensities using a ChemiGenius II system (PerkinElmer Life Sciences).

Crystallization—The purified StAP PSI protein sample was crystallized using the sitting-drop vapor diffusion method at 293 K using Qiagen PEG Suite screen solutions. The best crystals appeared in the drop containing 0.4 μl of protein solution, 0.2 μl of reservoir solution, equilibrated against 75 μl of reservoir solution (0.2 M lithium sulfate monohydrate, 20% polyethylene glycol 3350).

Diffraction Data Collection, Structure Solution, and Refinement—X-ray diffraction data for StAP PSI crystals were collected to 1.9 Å resolution using a Rigaku MicroMax 007HF rotating anode and a MAR345dtb system at a wavelength of 1.5418 Å. A data set was collected at 100 K using 25% (v/v) glycerol added to the reservoir solution as cryoprotectant. All data sets were indexed and integrated using the program XDS (41). Integrated intensities were converted to structure factors with modules F2MTZ and CAD of CCP4 (42). BUCCANEER (43) was used for initial automated model building. The structure was refined with REFMAC5 (44), rebuilt with COOT (45), and analyzed using PROCHECK (46) and COOT. Structural superpositions were performed using SSM (47) and ALIGN (48). Figures were generated using PyMOL (49) and UCSF Chimera (50).

Circular Dichroism (CD) Spectropolarimetry—CD analysis of PSI secondary structure was carried out using a Jasco J-810 spectropolarimeter (Jasco Inc., Easton, MD). 200 μl of 200 μg/ml PSI was loaded into a 1-mm path length quartz cell and scanned over 180–260 nm at 100 nm/min, 0.5-s response, standard sensitivity, and room temperature. Buffer 140 mM NaCl, 10 mM Tris-Cl, pH 7.4, or 140 mM NaCl, 20 mM MES, pH 4.5, was degassed under vacuum. For reducing condition effect determinations, DTT was added to final concentrations of 1.0, 2.5, and 5.0 mM, and heating was at 95 °C in a standard heating block for 5 min in a fume hood, followed by a 30-min cooling period on the bench top.

Preparation of Large Unilamellar Vesicles (LUVs)—LUVs were made of equimolar phosphatidylcholine (PC), phosphatidylethanolamine (PE) and/or phosphatidylserine (PS). To obtain 4 mM phospholipid (PL) suspensions, aliquots of 12.5 mg/ml PL stocks were mixed in a tube and dried under N_2 flush for at least 30 min and then suspended in 500 μl of 80 mM calcein, 140 mM NaCl, 10 mM HEPES, pH 7.4, by incubation at 37 °C with periodic sonication and vortexing over a minimum of 30 min. LUVs were prepared using a standard miniextruder (Avanti Polar Lipids, Alabaster, AL) containing a 100-nm pore membrane. The LUV prep was then desalted to remove untrapped calcein by gel filtration using a 5-ml HiTrap™ desalting column (GE Healthcare) and visual detection of free calcein in column. To quantify PL postdesalting, the micro-Bartlett phosphorous assay (51, 52) was used to determine the concentration of PLs based on inorganic phosphate content (53). Vesicle concentrations were calculated using PL concentrations, average vesicle diameter (140 nm), and the previously reported areas per lipid molecule: 59.7 Å^2 for PC (54), 57.4 Å^2 for PS, and 59.2 Å^2 for PE (55).

LUV Disruption Assays—PSI-caused perturbation of LUVs was measured by calcein leakage (56, 57) as detected using a Victor2 1420 Multilabel Counter (PerkinElmer Life Sciences) at 25 °C. 200-μl reactions were set up in 96-well microplates with varying concentrations of LUVs, 500 nM PSI, and either 140 mM NaCl, 10 mM HEPES, pH 7.4, or 140 mM NaCl, 20 mM MES, pH 4.5. Leakage was detected using excitation at 385 nm and emission at 435 nm with 3 s of shaking between readings. End points were measured by incubating LUVs in 0.5% Triton for each condition. Non-linear regression analyses were done using GraphPad Prism 4 (GraphPad Software Inc., La Jolla, CA).

Atomic Force Microscopy—A Veeco Picoforce multimode scanning probe microscope was used with a Nanoscope IV controller to image PE/PS membranes on the native oxide layer on silicon substrates. Images were collected in contact mode before and after the addition of PSI protein *in situ*. Suspensions of 3 mg/ml PE/PS vesicles were incubated on substrates for 60 min; rinsed with 100 μl of 140 mM NaCl, 20 mM MES, pH 4.5, to remove unfused material; and inserted into the fluid cell under 50 μl of buffer. Soft triangular cantilevers were used with spring constants between 0.02 and 0.03 newton/m, and the force applied during each scan was 1.5–2.0 nanonewtons. Scans of 5×5 μm were collected at a rate of 1.5 Hz, and 10×10-μm scans were collected at a rate of 0.75 Hz, corresponding to a tip velocity of 15.2 μm/s. After scanning the same region of substrate repeatedly over 30 min, 20 μl of 25 μM protein solution was injected directly into the buffer in the fluid cell, resulting in 7 μM PSI. Successive images were generated for a single region for time lapse data and for unscanned regions at the end of incubation, to assess changes to the membrane that were caused by repeated scanning of the AFM tip.

Particle Size Determination by Light Scattering—LUVs (100 μM) at pH 4.5 were incubated with PSI at room temperature and subjected to light scattering in a Malvern Zetasizer Nano-S (Malvern Instruments, Malvern, UK). A standard 1-ml cuvette was used containing 0.6 ml of sample that was allowed to equilibrate for a minimum of 15 min. Three consecutive measurements of five 30-s runs each were averaged using the refractive index for polystyrene, yielding the calculated average sizes and polydispersity indices.

RESULTS

Structure Solution and Refinement

Recombinant StAP PSI was expressed and purified to >98% purity with a typical yield of 5 mg/liter of culture, and its identity was verified by N-terminal sequencing (Advanced Protein Analysis Centre, Toronto, Canada). Diffraction data collection statistics are presented in Table 1. Crystals were hexagonal in space group $P3_221$ with unit cell parameters of $a = b = 56.47$, $c = 55.34$ Å. The Matthews coefficient (58) for the crystals was 2.24 Å^3 Da^{-1}, assuming the presence of one molecule in the asymmetric unit. StAP PSI exhibits a high level of sequence identity (53%) with the SAPLIP domain of prophytepsin PSI (Protein Data Bank code 1QDM; residues 4S–102S), which was used as a model for molecular replacement automated search by PHASER (59). The starting model consisted of a compact molecule and produced a weak solution. Analysis of the initial map showed that PHASER had placed only half of the initial model in a proper orientation despite good quality of the resulting electron density; however, there was sufficient density to accommodate the properly oriented half. At the next step, BUCCANEER (43) was used for automated model building, thereby producing the model of the StAP PSI structure with proper side chains for residues 59–100 and assigning the other residues as polyalanine. Iterative refinement of the partial model using REFMAC5 (44) and rebuilding in the electron density maps using COOT (45) produced the next model, which corresponded to an elongated, boomerang-shaped molecule.

TABLE 1
Data collection and refinement statistics

Parameters	Values
Data collection statistics[a]	
Space group	$P3_221$
Unit cell parameters *a, b, c* (Å)	56.47, 56.47, 55.34
Temperature (K)	100
Wavelength (Å)	1.5418
Resolution (Å)	40.0-190 (2.00-1.90)
R_{merge} (%)[b]	5.9 (90.0)
Completeness (%)	99.9 (100.0)
$I/\sigma(I)$	24.10 (2.87)
Unique reflections	8355 (1159)
Redundancy	10.32 (10.27)
No. of molecules/asymmetric unit	1
Refinement statistics	
Resolution (Å)	25.0–1.90
Working set	
No. of reflections	7936
R_{factor} (%)	18.7
Test set	
No. of reflections	417
R_{free} (%)	24.9
Protein atoms	633
No. of water molecules	63
Geometry statistics	
r.m.s. deviation (bond distance) (Å)	0.02
r.m.s. deviation (bond angle) (degrees)	1.81
Ramachandran plot[c]	
Most favored region (%)	98.6
Additionally allowed regions (%)	1.4
Generously allowed regions (%)	0.0
Disallowed regions (%)	0.0
Protein Data Bank code	3RFI

[a] The values in parentheses are for the highest resolution shell.
[b] $R_{merge} = \Sigma_h \Sigma_i |\langle I \rangle_h - I_{h,i}| / \Sigma_h \Sigma_i I_{h,i}$.
[c] As defined by PROCHECK.

When all of the residues visible in the electron density were built, translation-libration-screw parameters were introduced during the refinement. The overall anisotropy was modeled with translation-libration-screw parameters by dividing the molecule into three groups comprising residues 0–26, 27–82, and 83–103. The final model lacks residues 40–63, which could not be built due to insufficient electron density in this region of the crystal. The refinement statistics for the refined structure are presented in Table 1.

Tertiary and Quaternary Structures of StAP PSI

The overall fold of StAP PSI has a boomerang shape with an extended, open conformation (Fig. 1*A*) composed of four helices labeled H1–H4 (residues 1–24, 27–34, 66–82, and 85–99, respectively). H1 is connected to H4 via a disulfide linkage formed between Cys^6 and Cys^{99}, H3 is cross-linked to H2 via a disulfide bond between Cys^{31} and Cys^{71}, and Cys^{37} forms a disulfide bond with Cys^{68}. The tertiary structure is organized in such a way that one side (*top*) of the molecule is enriched with polar residues, and the other side (*bottom*) is enriched with hydrophobic residues (Fig. 1, *B* and *C*). Due to the crystallographic symmetry, two molecules form a very tight dimer (Fig. 1, *B* and *C*) with a buried surface area of 1746 $Å^2$, with the residues involved in the formation of the dimer interface being predominantly hydrophobic.

pH Dependence of Secondary Structure

Because PSI-induced membrane disruption requires acidic conditions (14), the secondary structures of StAP PSI at neutral and acidic pH were compared. CD scans were done in the same buffers used for all other experiments (*i.e.* 140 mM NaCl buffered by either 10 mM Tris-Cl (pH 7.4) or 20 mM Na-MES (pH 4.5)). Data below 195 nm were noisy, so secondary structure content could not be quantified. Qualitatively, the scans revealed spectra typical for high helix proteins (60); distinct negative absorption peaks occurred in the 220 and 208 nm spectral regions (Fig. 2). Helix content was higher overall at pH 4.5, similar to the pH dependence of influenza A hemagglutinin fusion peptide (61).

Secondary Structure Dependence on Disulfide Bonds

The structure of StAP PSI contains three disulfide bonds within its relatively small 12-kDa tertiary structure, and it was recently suggested that these cross-links are critical to PSI antimicrobial function (32). Hence, the dependence of PSI secondary structure on the presence of cystines was investigated. Fig. 3 contains the spectra of PSI at three concentrations of the reducing agent DTT, each with and without heating. No changes were observed for PSI heated at 95 °C under non-reducing conditions, indicating that native PSI secondary structural elements were heat-stable. DTT resulted in high interference at wavelengths below 200 nm, so its levels were limited to 5 mM or lower. Qualitatively from Fig. 3, a relatively minor loss of helix structure (220 and 208 nm negative peaks) occurred with the presence of reducing agent in an apparent dose-dependent manner. By contrast, when PSI was heated under reducing conditions, a more pronounced loss of secondary structure was observed, resulting in an approximate two-state structure change such that heating in 2.5 mM DTT resulted in a more dramatic loss of secondary structure. Further doubling of reducing agent concentration did not cause an equivalent effect, suggesting differential susceptibility of the respective disulfide bonds; the more robust cystine(s) were apparently critical to secondary structure stability of this predominantly helical structure.

Membrane Disruption Activity

Vesicle Leakage—LUVs containing self-quenching fluorophore (80 mM calcein) were used as substrate for the characterization of StAP PSI phospholipid bilayer disruption activity. Four combinations of PLs were tested at varying concentrations. Neutral vesicles made of 1:1 PC/PE were not affected by StAP PSI at any concentration tested, and none of the PL combinations were disrupted at neutral pH. By contrast, equimolar preparations of PS combined with PC and/or PE resulted in readily detectable activity, and leakage rates were calculated for 0.5 μM PSI over the PL concentration range 20–500 μM. Accurate LUV disruption rate determinations above 500 μM were prevented by excessive fluorescence signal, and the quality of determinations below 20 μM was limited by excessive background noise levels due to untrapped calcein. Rate determinations were calculated relative to PL concentrations in units of μM/min (in terms of both PL and LUV concentration) and yielded initial rates with low relative errors. PSI-induced lipid bilayer disruption varied non-linearly with PL/LUV concentration, and the order of leakage rates was PE/PS > PC/PS > PE/PC/PS within the concentration range tested (Fig. 4).

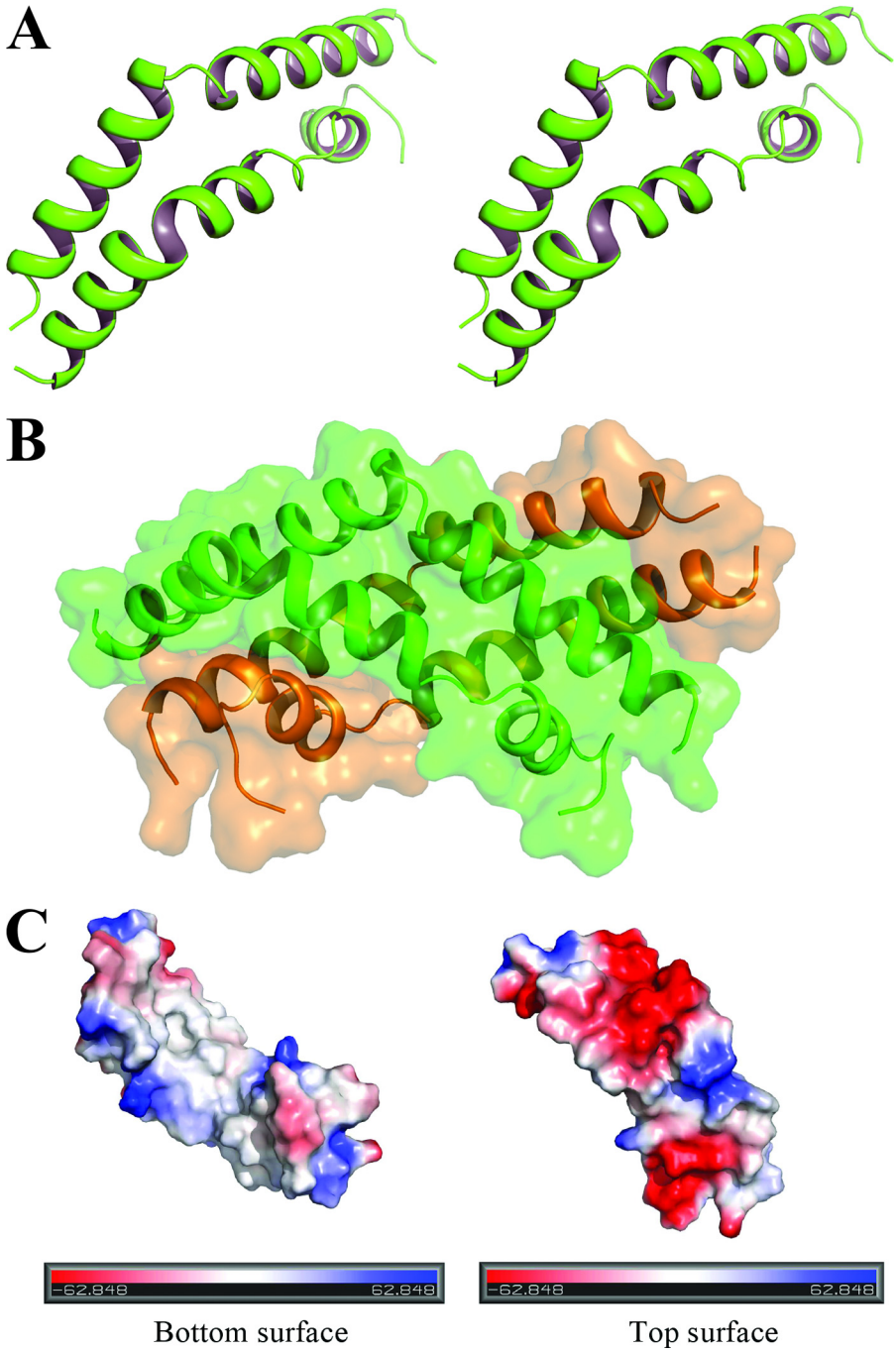

FIGURE 1. *A*, stereo view of the StAP PSI monomeric structure. The structure is shown in a *ribbon representation*. *B*, crystallographic dimer of StAP PSI; two molecules are shown as *ribbons* inside the transparent surface of the dimer. *C*, electrostatic surface representation of the StAP PSI structure.

Non-linear regression analyses for both one-phase exponential association and the Michaelis-Menten equation were compared by F-tests using GraphPad Prism 4, and the independent data sets for all three PL combinations fit better to the Michaelis-Menten model. Table 2 summarizes the kinetic results, including goodness of fit parameters for the regression analyses. Because the mechanism of action has not been characterized (see "Discussion"), apparent Michaelis constants (K_m) were not reported because their meaning in terms of substrate affinity would be undefined in the absence of understanding the relative dissociation rates of PSI and PL in original bilayer (reactant; k_{-1}) and displaced PL in new environment (product; k_2). A lack of data at higher lipid concentrations (which produced excessive fluorescence signals) resulted in a relatively large turnover number S.E. value for PC/PS. LUV concentrations above 500 μM would allow for more precise kinetic parameter determinations and will require further characterization. Nevertheless, the overall fit to the model was good for each data set, including that for PC/PS ($R^2 = 0.99$).

Atomic Force Microscopy—AFM height images of PE/PS bilayers were collected using contact mode as described under "Experimental Procedures." LUVs were incubated on the surface of the native oxide layer on a silicon wafer in the same buffer used for LUV disruption assays for 1 h, resulting in

bilayer fusion to the substrate surface. The fused membrane was organized as 5-nm-high islands that were ~100 nm wide, dispersed across the substrate (Fig. 5*A*, *top*). The bilayer height was within the expected range (35, 62), and repeated scans in contact mode over a single region did not change the bilayer morphology significantly. Upon PSI injection, membrane patches fused to form larger regions of uniform membrane separated by larger membrane-free areas (Fig. 5*A*, *bottom*). Additionally, 20–50-nm-high lipid islands formed in regions unperturbed by the AFM tip (Fig. 5*B*, *right*); thus, PSI appeared to induce fusion of membrane patches as evidenced by bilayer rearrangement in areas that were not repeatedly scanned. Such formations did not occur on regions subjected to successive scanning; on these regions, considerable smoothing of the membrane occurred. PSI apparently softened or lubricated bilayers, allowing them to be displaced by the AFM tip upon repeated scanning. Fig. 5*B* (*right*) shows the distinct effects of PSI both with (*center square region*) and without (*surrounding region*) repeated AFM tip scanning. Large regions of 5-nm-high bilayer were observed after eight scans on a single region, whereas repeated scanning in the absence of PSI did not result in similar bilayer rearrangement.

Light Scattering—LUVs (100 μM) at pH 4.5 were incubated with PSI at room temperature, and particle size was measured by light scattering in a Malvern Zetasizer Nano-S (Malvern Instruments); results are summarized in Table 3. After 60 min at a PSI concentration equivalent to LUV disruption assays (0.5 μM), average particle size slightly increased, and a concomitant increase in the polydispersity index (mass distribution) was more pronounced (Table 3). By 100 min, average particle size had increased by nearly two-thirds (65%), and the polydispersity index had more than tripled. Higher PSI concentration (4 μM) was assayed to further investigate the peak area tendency toward higher vesicle size. After just 15 min equilibration time post-PSI addition, average particle size and polydispersity index had not only increased more than for the entire 0.5 μM PSI assay, but a newly formed, larger vesicle size (1510 nm) accounting for one-third of the total peak area was observed. Together with the above AFM results, vesicle size measurements indicated that PSI activity resulted in lipid bilayer fusion.

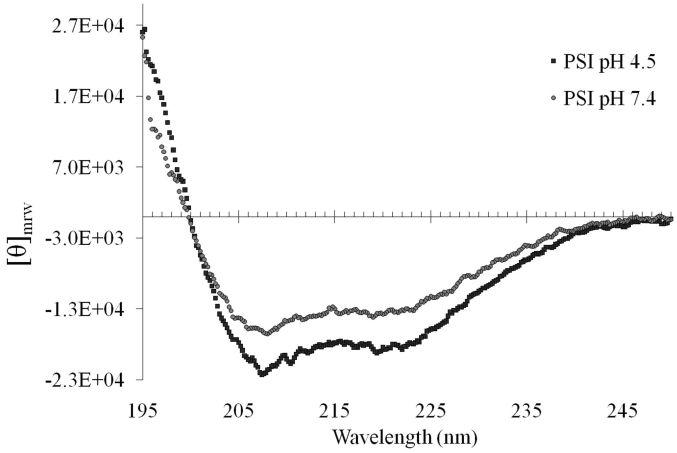

FIGURE 2. **Effect of acidification on StAP PSI secondary structure; far-UV CD spectra at pH 4.5 (*red squares*) and pH 7.4 (*shaded circles*) in 140 mM NaCl.**

DISCUSSION

Structural Comparison—The overall fold of StAP PSI is similar to the open, extended form of human saposin C (Fig. 6*A*) as observed in the tetragonal crystal structure (63). The structure of StAP PSI has been compared with the PSI domain of plant phytepsin (9), revealing that the r.m.s. deviation for 38 aligned C_α atoms is 0.9 Å. Overall, superposition of a pseudomonomer StAP PSI structure (constructed from its dimer crystal structure) onto the PSI of phytepsin produced an r.m.s. deviation of 1.4 Å (71 C_α pairs). Helices H1 and H4 of StAP PSI were superimposable with the equivalent helices of phytepsin PSI (Fig. 6*A*), whereas helices H2 and H3 from the second StAP PSI molecule in the crystallographic dimer superimpose onto helices H2 and H3 of phytepsin PSI. This result clearly shows that the crystallographic dimer structure of StAP PSI is composed of two extended, domain-swapped monomers. The StAP PSI structure has also been compared with three different crystal structures of human saposin C (Fig. 6*A*). The C_α atoms of res-

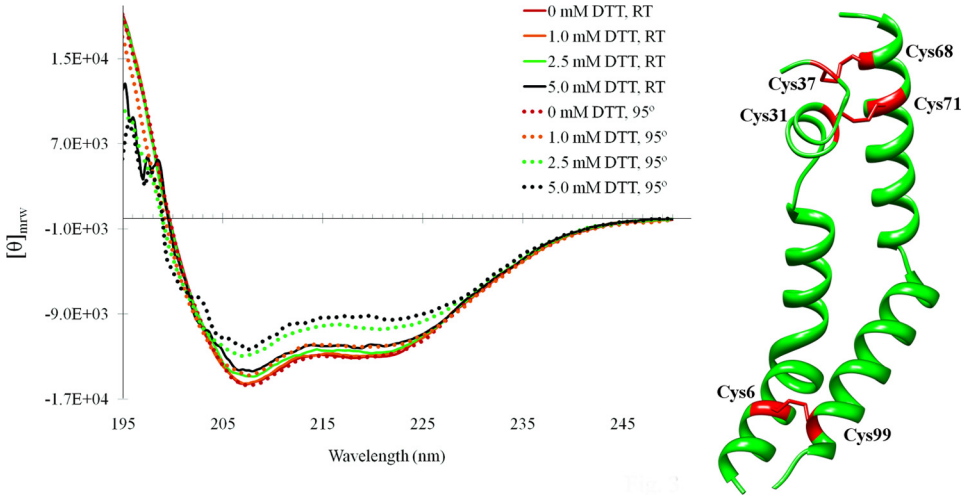

FIGURE 3. **Importance of disulfide bonds on StAP PSI secondary structure; far-UV CD spectra of StAP PSI at varying concentrations of reducing agent DTT with (*dotted lines*) and without (*solid lines*) heating.** The locations of the various disulfide bonds are indicated (*red*) in the accompanying structure.

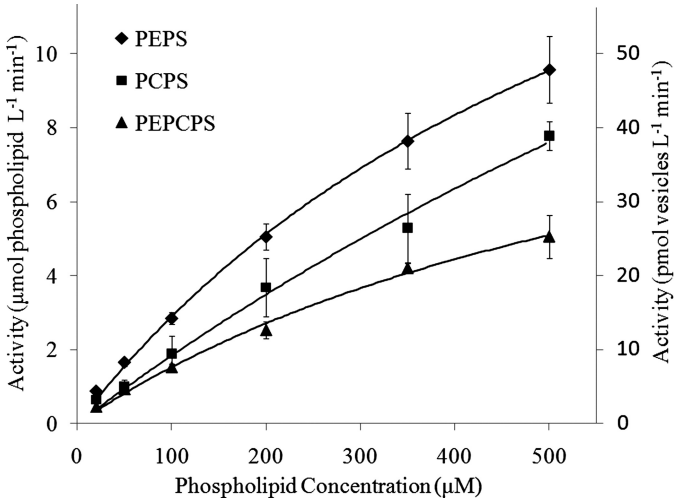

FIGURE 4. **Kinetics of LUV disruption by 0. 5 μM StAP PSI at 25 °C; comparison of three acidic phospholipid mixtures (activity against non-acidic PE/PC was not detectable).** Two *vertical axes* are presented for disruption rates in terms of both phospholipid concentration (*left axis*) and vesicle concentration (*right axis*). *Error bars*, S.E.

TABLE 2

Turnover and goodness of fit to the Michaelis-Menten model for StAP PSI-induced vesicle leakage

Data are shown relative to both phospholipid and vesicle concentrations.

Phospholipid composition	$k_{cat(app)}$ (phospholipid)	$k_{cat(app)}$ (vesicle)	R^2
	min^{-1}	$\times 10^{-4}\ min^{-1}$	
PC/PS	71 ± 30	3.6 ± 2	0.992
PE/PS	45 ± 3	2.3 ± 0.2	0.999
PE/PC/PS	25 ± 4	1.3 ± 0.2	0.996

idues 6–19 from saposin C were superimposed (LSQ) to the C_α atoms of the first 13 residues of the StAP PSI structure, yielding an r.m.s. deviation of 0.6 Å (tetragonal crystal form, Protein Data Bank code 2Z9A), 0.6 Å (orthorhombic crystal form, Protein Data Bank code 2QYP) and 0.9 Å (hexagonal crystal form, Protein Data Bank code 2GTG). This "open" conformation for SAPLIPs has also been observed for saposin B (Protein Data Bank code 1N69), and all three structures are shown side by side in Fig. 6*B*.

Saposin-like Activity—StAP PSI-liposome disruption rates varied with PL/LUV concentration in a non-linear fashion, and, to our knowledge, the present study is the first to characterize the kinetic activity of a SAPLIP for varying PL/LUV concentrations of multiple PL compositions, revealing Michaelis-Menten-like kinetics. In attempting to elucidate the nature of PSI activity, AFM results suggested that StAP PSI caused pronounced rearrangement of acidic PL bilayers under the same conditions used for liposome disruption. The type of lipid structures that formed were similar to those previously characterized for saposin C, which showed that saposin C interactions with PL bilayers (64) resulted in rearrangement of membrane patches of increased thickness and membrane destabilization (35, 64). Saposin C has also been shown to cause vesicle fusion (65), which involves insertion of the terminal helices into the membrane where saposin-membrane and saposin-saposin interactions carry out a "clip-on" mechanism at neutral and acidic pH. Saposin C causes fusion when present at as little as 0.05 μM and produced fused vesicles up to 3000 nm (29).

By contrast, saposin B displays fusogenic activity only against anionic vesicles and exclusively at acidic pH and induces only minor vesicle size increases at protein concentrations of 1 μM or below. However, at 2 μM, saposin B induces more significant vesicle fusion, yielding an average product ~1800 nm in diameter (29). The fusogenic results for StAP PSI in the present study were strikingly similar in that 0.5 μM PSI induced only minor average diameter increases, whereas 4 μM PSI induced dramatic changes, resulting in new lipid structures averaging 1510 nm (Table 3). Also similar to StAP PSI disruption and AFM observations, saposins B and D disrupt anionic membranes in a pH-dependent process where they solubilize (30, 66) and mobilize (30) lipids. Furthermore, saposin B binds and transfers PLs of anionic membranes such that it has a preference for PC transfer (28). Although StAP PSI-mediated vesicle disruption rates were all higher for PE/PS within the concentration range used in the present study, kinetic analysis suggested a higher maximum velocity for PC/PS disruption ($p = 0.06$), indicating a PL preference similar to saposin B. Perhaps the bulkier choline substituent, relative to ethanolamine, results in more favorable PSI interactions with the bilayer surface and/or results in different bilayer packing density. A study of the nature of SAPLIP PL preference is under way.

The crystal structure of saposin B with bound lipid indicated that PLs interact with the dimeric form of the protein. Dimerization occurs via clasping together two V-shaped protein monomers, thereby forming a shell-like monolayer of α-helices with a long interface that buries a relatively large hydrophobic cavity (33). A similar V-shape and quaternary structural arrangement was observed in the present study for the StAP PSI crystal structure, although PSI and open saposin C contain a more obtuse angle in their boomerang shape relative to saposin B (see Fig. 6*B*), according to structural alignments. Furthermore, PSI membrane effects as detected by AFM were in partial agreement with saposin B in that new lipid structures formed that were higher than the surrounding bilayers; structures observed for saposin B were smaller in size, however (35). These newly formed "granules" could be dislodged by the scanning AFM tip, indicating that they were loosely bound upon saposin B action (35). Similarly, raised lipid bilayers acted upon by StAP PSI became more fluid in regions repeatedly scanned by the AFM tip and were spread out into smooth continuous lipid regions (Fig. 5*B*), indicating solubilizing and/or mobilizing activity.

Plant AP PSI Activity—Recombinant StAP PSI is toxic to plant (*Phytophthora infestans* and *Fusarium solani*) and human (*Staphylococcus aureus*, *Bacillus cereus*, and *E. coli*) pathogens, and it permeabilizes their plasma membranes (32). In both procardosin A and StAP, the PSI has been confirmed to be responsible for membrane interactions (14, 32). The interaction of procardosin A PSI with membrane vesicles is pH-dependent and varies with lipid composition (14), in agreement with the present study. Interestingly, the only other crystal structure for a plant AP PSI, prophytepsin, was shown to have a tertiary structure consisting of the "closed" saposin fold (9). That crystal structure dealt with a PSI attached to its parent zymogen molecule and contrasts with the "open" saposin fold observed in the present study for a PSI independent of its zymogen source. By definition, fusogenic activity via the "clip-on" mechanism (29)

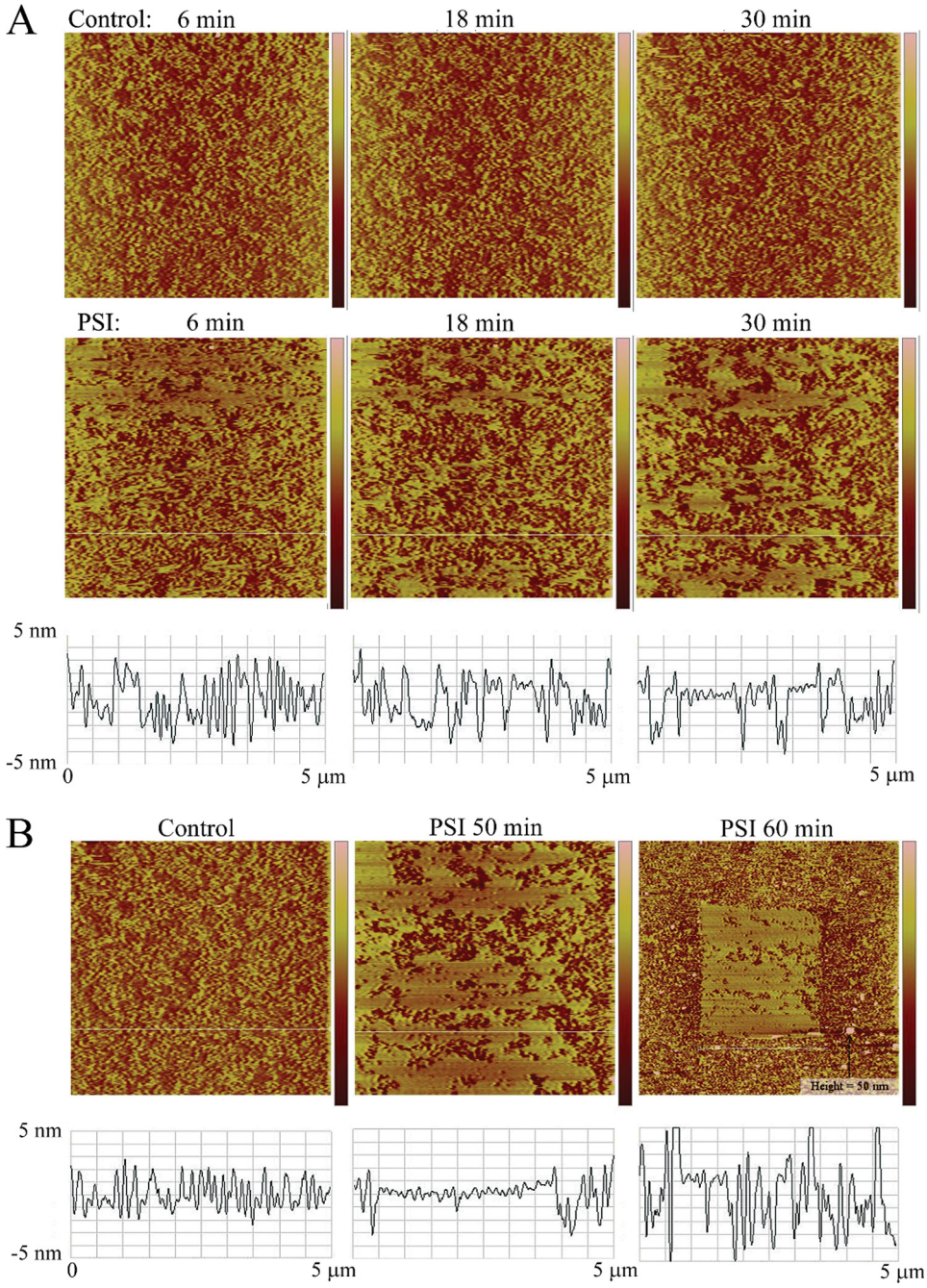

FIGURE 5. **AFM height images of PE/PS bilayer patches at pH 4.5 on the native oxide layer of a silicon wafer.** *A*, *top*, successive scans without PSI (*left* to *right*); the membrane is patchy, with ~100-nm-wide islands of height 5 nm. *Bottom*, successive scans with PSI (*left* to *right*); the membrane is smooth, transforming from patchy islands to large continuous membrane. The *white lines* indicate height sections shown *below* each *image*. *B*, AFM *height images* of the same region as in *A*. *Left*, preinjection; *middle*, 50 min (eighth scan) postinjection; *right*, 60 min (ninth scan) postinjection showing a larger region *zoomed out* to twice the scan width. Note the smoothing of the membrane over the region repeatedly scanned by the AFM tip postinjection and the appearance of islands much taller (*white*) than the original 5-nm bilayer height in the region not affected by repeated scanning of the AFM tip.

is dependent upon open structure dimerization (interfacing of the respective hydrophobic surfaces). Thus, we propose that plant AP PSIs probably change from closed to open fold upon release from the parent AP molecule, thereby facilitating bilayer interaction and subsequent protein quaternary structure dimerization, yielding fusion of neighboring bilayer structures.

The cytotoxicity and plasma membrane interactions of StAP PSI were previously shown to be dependent on its secondary and/or tertiary structure, as evidenced by loss of activity upon DTT treatment (32). In the present study, CD scans at 1 mM DTT resulted in no apparent spectral change, and only minor changes were indicated at DTT concentrations up to 5 mM (without heating). This suggested that disulfide bonds are not critical to PSI secondary structure under normal temperature conditions. When synthetic peptides equivalent to the individual helices of saposin C (*i.e.* no native tertiary structure) were studied, bilayer fusogenic activity was not observed (29), sug-

TABLE 3
Effect of StAP PSI on LUV size at pH 4.5

	Time	*Z*-average size	Polydispersity index
	min	*nm*	
0.5 μM StAP PSI	0	142 ± 0.85	0.0870 ± 0.020
	60	146 ± 1.6	0.172 ± 0.018
	100	235 ± 0.20	0.300 ± 0.0030
4 μM StAP PSI	0	137 ± 1.2	0.0737 ± 0.0098
	15 (overall)	257 ± 4.4	0.529 ± 0.064
	15 (peak 1)	167 ± 11	(65% ± 1 of total area)
	15 (peak 2)	1510 ± 300	(34% ± 1 of total area)

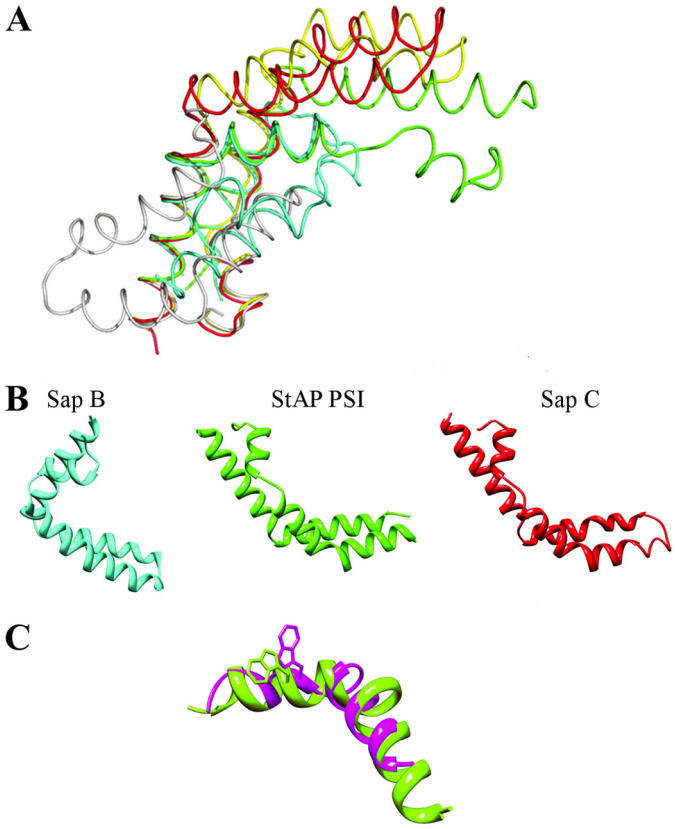

FIGURE 6. *A*, structural superposition of StAP PSI (*green*) with the plant-specific insert domain of prophytepsin (*cyan*), tetragonal (*yellow*), hexagonal (*gray*), and orthorhombic (*red*) crystal forms of saposin C. *B*, side by side comparison of the "open" saposin boomerang fold of saposin B (Protein Data Bank code 1N69), saposin C (Protein Data Bank code 2QYP), and StAP PSI (Protein Data Bank code 3RFI). *C*, pairwise structural alignment of influenza A hemagglutinin fusion peptide (1IBN; *purple*) superimposed over StAP PSI (3RFI; *green*) using UCSF Chimera version 1.5.2 implementing the Needleman-Wunsch algorithm. The overall r.m.s. deviation was 2.013 Å for 19 residues that aligned, ignoring gaps.

gesting a critical role of tertiary structure in SAPLIP-catalyzed bilayer fusion. Because cystines are critical to antimicrobial function (32), their role must be to maintain tertiary structure required for fusogenic activity.

Additionally, the DTT titration CD experiment indicated that the disulfide bonds conferred stability to PSI secondary structures, as evidenced by a much more pronounced CD spectral change for heat-treated PSI. The latter was superimposable with that for the non-reducing, unheated sample (Fig. 3), indicating that the PSI disulfide bonds apparently protected the individual helices from heat denaturation. Since both open and closed forms of SAPLIPs contain the same disulfide bonds (15), the primary role of PSI cystines is probably not to maintain the overall fold but perhaps to confer rigidity. Fusion of adjacent membranes consists of the displacement of lipid from its stable, energetically favorable bilayer environment to an aqueous, high energy intermediate state, and such a transition requires enzymatic action (67). Perhaps the energy required to catalyze this event is related to multimer formation (68) and conformation changes (69, 70) related to PSI rigidity/stability dependent on disulfide bonds.

Fusogenic Mechanism—There is a correlation between the ability of a fusion peptide to adopt a helical configuration and its ability to promote membrane fusion (71). In addition to saposins, the formation of dimers via complexing of stable, predominantly helical structures is a protein structure scheme common to yeast SNARE-mediated membrane fusion (72, 73) as well as viral fusases that are derived from larger precursors that require proteolytic processing to potentiate their fusion activity (71). These associations of α-helices contain one hydrophobic face, an arrangement similar to StAP PSI with its five helices, hydrophobic inner cavity, and N terminus. An important fusase fusion peptide for virus-cell fusion is the N-terminal portion of influenza A hemagglutinin, which adopts an α-helical conformation in lipid bilayers (74), constitutes an autonomous folding unit in the membrane, and catalyzes lipid exchange between juxtaposed membranes (61).

In some plant APs, the release of PSI occurs via proteolytic cleavage upon acid-induced autoactivation of the precursor protein and subsequent processing, albeit via self-cleavage (6, 8, 75). Interestingly, influenza A hemagglutinin fusion peptide is inaccessible to membranes at neutral pH; however, a drop of the pH inside the endosome below a critical threshold induces a large conformational change in the parent protein and is subsequently activated by a protease (plasmin) that cleaves the precursor polypeptide (76) into two disulfide-linked polypeptides and a fusion peptide (77). The hemagglutinin fusion peptide has a slightly higher helix content at pH 5 than at pH 7.4, as revealed by comparison of CD spectra (61, 74), which are remarkably similar to those for StAP PSI in the present study (Fig. 2) in terms of overall shape (dominant helix content) as well as their *x* intercepts and superimposed relative spectra (gain of helical structure upon acidification). In addition, the fold of the hemagglutinin fusion peptide (61) is similar to the StAP PSI structure reported here as well as to saposins (78); structural alignment of the N terminus of hemagglutinin fusion peptide (Protein Data Bank code 1IBN) (61) with the N terminus of StAP PSI revealed similar (r.m.s. deviation 1.43 Å for 9 C_α carbons) helix-kink-helix folds (Fig. 6*C*). The tryptophan within the hemagglutinin fusion peptide has been shown to induce its characteristic boomerang shape (26), which is critical to the fusogenic and membrane-disrupting activities of this fold (79). Alignment of StAP PSI with hemagglutinin fusion peptide suggested a similar role for the critical tryptophan residue (Fig. 6*C*). In this context, the likely protein structural reason for the acidic pH requirement of AP PSI-membrane interactions is the existence of acid-induced helical structure critical for membrane interaction.

Fusase within a Protease—The apparent sharing of a common hydrophobic region fold that is subject to similar pH-dependent secondary structure changes required for membrane

fusion suggests a common mode of action. Perhaps this helix-kink-helix fold is universal (*i.e.* saposins in animals, hemagglutinin in viruses, and APs in plants) in its membrane fusogenic nature, extending functionality across various species and kingdoms. Collectively, the findings that a plant AP domain displays fusase-like activity (liposome disruption, bilayer solubilization/lubrication, and bilayer fusion) as well as fusase-like structure-function character (inter- and intramolecular helix oligomer association, hemagglutinin fusion peptide-like fold, hydrophobic helix end region, and pH dependence of secondary structure-activity) lead to the conclusion that they are indeed fusase-like proteins, acting as discrete entities.

Considering the myriad proteins that have more than one function, the idea of one gene, one protein, one function is insufficient in the study of proteins (80). Recently, a bifunctional AP has been engineered (81); however, no reports have characterized cases of AP "moonlighting" (82) (*i.e.* serving an additional function beyond the main enzymatic reaction) (83), and only one moonlighting plant peptidase (mitochondrial processing peptidase) has been reported (82, 84). In this case, the multiple functions arise from a singular structural fold (85), whereas PSIs are structurally unrelated to their AP "hosts" (*i.e.* the PSI domain of a plant AP has apparent enzymatic activity and is independent of its "parent" proenzyme, which has its own distinct class of enzymatic activity). Thus, the saposin-like domains of plant APs present a unique case: a distinct, functionally unrelated domain within the primary structure of another domain (the C-terminal domain) of its enclosing protein. Fusase activity from within a protease sequence presents, to our knowledge, the first confirmation and characterization of an independently acting "enzyme within an enzyme."

Acknowledgments—We thank Lauren Agro, Joseph Chu, and Dr. Frances Sharom for assistance.

REFERENCES

1. Davies, D. R. (1990) *Annu. Rev. Biophys. Biophys. Chem.* **19,** 189–215
2. Blundell, T. L., and Johnson, M. S. (1993) *Protein Sci.* **2,** 877–883
3. Guevara, M. G., Oliva, C. R., Huarte, M., and Daleo, G. R. (2002) *Eur. J. Plant Pathol.* **108,** 131–137
4. Schaller, A., and Ryan, C.,A. (1996) *Plant Mol. Biol.* **31,** 1073–1077
5. Payie, K. G., Weadge, J. T., Tanaka, T., and Yada, R. Y. (2000) *Biotechnol. Lett.* **22,** 1515–1520
6. Glathe, S., Kervinen, J., Nimtz, M., Li, G. H., Tobin, G. J., Copeland, T. D., Ashford, D. A., Wlodawer, A., and Costa, J. (1998) *J. Biol. Chem.* **273,** 31230–31236
7. Payie, K. G., Tanaka, T., Gal, S., and Yada, R. Y. (2003) *Biochem. J.* **372,** 671–678
8. Ramalho-Santos, M., Veríssimo, P., Cortes, L., Samyn, B., Van Beeumen, J., Pires, E., and Faro, C. (1998) *Eur. J. Biochem.* **255,** 133–138
9. Kervinen, J., Tobin, G. J., Costa, J., Waugh, D. S., Wlodawer, A., and Zdanov, A. (1999) *EMBO J.* **18,** 3947–3955
10. Frazão, C., Bento, I., Costa, J., Soares, C. M., Veríssimo, P., Faro, C., Pires, E., Cooper, J., and Carrondo, M. A. (1999) *J. Biol. Chem.* **274,** 27694–27701
11. Mazorra-Manzano, M. A., Tanaka, T., Dee, D. R., and Yada, R. Y. (2010) *Phytochemistry* **71,** 515–523
12. Mutlu, A., and Gal, S. (1999) *Physiol. Plant.* **105,** 569–576
13. Runeberg-Roos, P., Törmäkangas, K., and Ostman, A. (1991) *Eur. J. Biochem.* **202,** 1021–1027
14. Egas, C., Lavoura, N., Resende, R., Brito, R. M., Pires, E., de Lima, M. C., and Faro, C. (2000) *J. Biol. Chem.* **275,** 38190–38196
15. Bruhn, H. (2005) *Biochem. J.* **389,** 249–257
16. Kolter, T., and Sandhoff, K. (2005) *Annu. Rev. Cell Dev. Biol.* **21,** 81–103
17. Matsuda, J., Vanier, M. T., Saito, Y., Tohyama, J., Suzuki, K., and Suzuki, K. (2001) *Hum. Mol. Genet.* **10,** 1191–1199
18. Anderson, D. H., Sawaya, M. R., Cascio, D., Ernst, W., Modlin, R., Krensky, A., and Eisenberg, D. (2003) *J. Mol. Biol.* **325,** 355–365
19. Liepinsh, E., Andersson, M., Ruysschaert, J. M., and Otting, G. (1997) *Nat. Struct. Biol.* **4,** 793–795
20. Gordon, L. M., Lee, K. Y., Lipp, M. M., Zasadzinski, J. A., Walther, F. J., Sherman, M. A., and Waring, A. J. (2000) *J. Pept. Res.* **55,** 330–347
21. Zhai, Y., and Saier, M. H., Jr. (2000) *Biochim. Biophys. Acta* **1469,** 87–99
22. Stiasny, K., Kössl, C., Lepault, J., Rey, F. A., and Heinz, F. X. (2007) *PLoS Pathog.* **3,** e20
23. Kasson, P. M., Lindahl, E., and Pande, V. S. (2010) *PLoS Comput. Biol.* **6,** e1000829
24. Bissonnette, M. L., Donald, J. E., DeGrado, W. F., Jardetzky, T. S., and Lamb, R. A. (2009) *J. Mol. Biol.* **386,** 14–36
25. Qiao, H., Armstrong, R. T., Melikyan, G. B., Cohen, F. S., and White, J. M. (1999) *Mol. Biol. Cell* **10,** 2759–2769
26. Lai, A. L., Park, H., White, J. M., and Tamm, L. K. (2006) *J. Biol. Chem.* **281,** 5760–5770
27. Lukatsky, D. B., and Frenkel, D. (2004) *Eur. Phys. J. E* **14,** 3–6
28. Ciaffoni, F., Tatti, M., Boe, A., Salvioli, R., Fluharty, A., Sonnino, S., and Vaccaro, A. M. (2006) *J. Lipid Res.* **47,** 1045–1053
29. Wang, Y., Grabowski, G. A., and Qi, X. (2003) *Arch. Biochem. Biophys.* **415,** 43–53
30. Remmel, N., Locatelli-Hoops, S., Breiden, B., Schwarzmann, G., and Sandhoff, K. (2007) *FEBS J.* **274,** 3405–3420
31. Simoes, I., and Faro, C. (2004) *Eur. J. Biochem.* **271,** 2067–2075
32. Muñoz, F. F., Mendieta, J. R., Pagano, M. R., Paggi, R. A., Daleo, G. R., and Guevara, M. G. (2010) *Peptides* **31,** 777–785
33. Ahn, V. E., Faull, K. F., Whitelegge, J. P., Fluharty, A. L., and Privé, G. G. (2003) *Proc. Natl. Acad. Sci. U.S.A.* **100,** 38–43
34. Ahn, V. E., Leyko, P., Alattia, J. R., Chen, L., and Privé, G. G. (2006) *Protein Sci.* **15,** 1849–1857
35. Alattia, J. R., Shaw, J. E., Yip, C. M., and Privé, G. G. (2006) *J. Mol. Biol.* **362,** 943–953
36. Ghannoum, M. A., and Rice, L. B. (1999) *Clin. Microbiol. Rev.* **12,** 501–517
37. Meyer, V. (2008) *Appl. Microbiol. Biotechnol.* **78,** 17–28
38. Tseng, H. K., and Perfect, J. R. (2011) *Expert Opin. Pharmacother.* **12,** 241–256
39. Hanahan, D. (1983) *J. Mol. Biol.* **166,** 557–580
40. Laemmli, U. K. (1970) *Nature* **227,** 680–685
41. Kabsch, W. (1993) *J. Appl. Crystallogr.* **26,** 795–800
42. CCP4 (1994) *Acta Crystallogr. D* **50,** 760–763
43. Cowtan, K. (2006) *Acta Crystallogr. D* **62,** 1002–1011
44. Murshudov, G. N., Vagin, A. A., and Dodson, E. J. (1997) *Acta Crystallogr. D* **53,** 240–255
45. Emsley, P., and Cowtan, K. (2004) *Acta Crystallogr. D* **60,** 2126–2132
46. Laskowski, R. A., MacArthur, M. W., Moss, D. S., and Thornton, J. M. (1993) *J. Appl. Crystallogr.* **26,** 283–291
47. Krissinel, E., and Henrick, K. (2004) *Acta Crystallogr. D* **60,** 2256–2268
48. Cohen, G. E. (1997) *J. Appl. Crystallogr.* **30,** 1160–1161
49. DeLano, W. L. (2002) *The PyMOL Molecular Graphics System Version 1.2,* DeLano Scientific LLC, San Carlos, CA
50. Pettersen, E. F., Goddard, T. D., Huang, C. C., Couch, G. S., Greenblatt, D. M., Meng, E. C., and Ferrin, T. E. (2004) *J. Comput. Chem.* **25,** 1605–1612
51. Bartlett, G. R. (1959) *J. Biol. Chem.* **234,** 466–468
52. Fiske, C. H., and Subbarow, Y. (1925) *J. Biol. Chem.* **66,** 375–400
53. Sharom, F. J., DiDiodato, G., Yu, X., and Ashbourne, K. J. (1995) *J. Biol. Chem.* **270,** 10334–10341
54. Petrache, H. I., Tristram-Nagle, S., and Nagle, J. F. (1998) *Chem. Phys. Lipids* **95,** 83–94
55. Huster, D., Arnold, K., and Gawrisch, K. (2000) *Biophys. J.* **78,** 3011–3018
56. MacDonald, R. C., MacDonald, R. I., Menco, B. P., Takeshita, K., Subbarao, N. K., and Hu, L. R. (1991) *BBA-Biomembranes* **1061,** 297–303

57. Matsuzaki, K., Harada, M., Handa, T., Funakoshi, S., Fujii, N., Yajima, H., and Miyajima, K. (1989) *BBA-Biomembranes* **981,** 130–134
58. Matthews, B. W. (1968) *J. Mol. Biol.* **33,** 491–497
59. Read, R. J. (2001) *Acta Crystallogr. D* **57,** 1373–1382
60. Sreerama, N., and Woody, R. W. (2004) *Methods Enzymol.* **383,** 318–351
61. Han, X., Bushweller, J. H., Cafiso, D. S., and Tamm, L. K. (2001) *Nat. Struct. Biol.* **8,** 715–720
62. Egawa, H., and Furusawa, K. (1999) *Langmuir* **15,** 1660–1666
63. Rossmann, M., Schultz-Heienbrok, R., Behlke, J., Remmel, N., Alings, C., Sandhoff, K., Saenger, W., and Maier, T. (2008) *Structure* **16,** 809–817
64. You, H. X., Qi, X., Grabowski, G. A., and Yu, L. (2003) *Biophys. J.* **84,** 2043–2057
65. Vaccaro, A. M., Tatti, M., Ciaffoni, F., Salvioli, R., Serafino, A., and Barca, A. (1994) *FEBS Lett.* **349,** 181–186
66. Ciaffoni, F., Salvioli, R., Tatti, M., Arancia, G., Crateri, P., and Vaccaro, A. M. (2001) *J. Biol. Chem.* **276,** 31583–31589
67. Baker, D., and Agard, D. A. (1994) *Structure* **2,** 907–910
68. Markovic, I., Pulyaeva, H., Sokoloff, A., and Chernomordik, L. V. (1998) *J. Cell Biol.* **143,** 1155–1166
69. Kingsley, D. H., Behbahani, A., Rashtian, A., Blissard, G. W., and Zimmerberg, J. (1999) *Mol. Biol. Cell* **10,** 4191–4200
70. Chernomordik, L. V., Frolov, V. A., Leikina, E., Bronk, P., and Zimmerberg, J. (1998) *J. Cell Biol.* **140,** 1369–1382
71. Hernandez, L. D., Hoffman, L. R., Wolfsberg, T. G., and White, J. M. (1996) *Annu. Rev. Cell Dev. Biol.* **12,** 627–661
72. Paumet, F., Rahimian, V., and Rothman, J. E. (2004) *Proc. Natl. Acad. Sci. U.S.A.* **101,** 3376–3380
73. Paumet, F., Rahimian, V., Di Liberto, M., and Rothman, J. E. (2005) *J. Biol. Chem.* **280,** 21137–21143
74. Han, X., and Tamm, L. K. (2000) *Proc. Natl. Acad. Sci. U.S.A.* **97,** 13097–13102
75. Faro, C., Ramalho-Santos, M., Vieira, M., Mendes, A., Simões, I., Andrade, R., Veríssimo, P., Lin, X., Tang, J., and Pires, E. (1999) *J. Biol. Chem.* **274,** 28724–28729
76. Lazarowitz, S. G., Goldberg, A. R., and Choppin, P. W. (1973) *Virology* **56,** 172–180
77. Gray, C., Tatulian, S. A., Wharton, S. A., and Tamm, L. K. (1996) *Biophys. J.* **70,** 2275–2286
78. Vaccaro, A. M., Salvioli, R., Barca, A., Tatti, M., Ciaffoni, F., Maras, B., Siciliano, R., Zappacosta, F., Amoresano, A., and Pucci, P. (1995) *J. Biol. Chem.* **270,** 9953–9960
79. Lai, A. L., and Tamm, L. K. (2010) *J. Biol. Chem.* **285,** 37467–37475
80. Jeffery, C. J. (2009) *Mol. Biosyst.* **5,** 345–350
81. Bryksa, B. C., Horimoto, Y., and Yada, R. Y. (2010) *Protein Eng. Des. Sel.* **23,** 711–719
82. Moore, B. D. (2004) *Trends Plant Sci.* **9,** 221–228
83. Copley, S. D. (2003) *Curr. Opin. Chem. Biol.* **7,** 265–272
84. Braun, H. P., and Schmitz, U. K. (1999) *Planta* **209,** 267–274
85. Braun, H. P., and Schmitz, U. K. (1995) *Trends Biochem. Sci.* **20,** 171–175